Ensemble RBS: Probing the compositional profile of 3D microscale structures

Niels Claessens [a,b,*], Pierre Couture [c], Jonathan England [c], Rita Vos [a], Thomas Hantschel [a], Wilfried Vandervorst [a,b], André Vantomme [b], Johan Meersschaut [a]

[a] *IMEC, Kapeldreef 75, Leuven 3001, Belgium*
[b] *Quantum Solid State Physics, KU Leuven, Celestijnenlaan 200D, Leuven 3001, Belgium*
[c] *Ion Beam Centre, University of Surrey, Guildford, Surrey GU2 7XH, United Kingdom*

ABSTRACT

Rutherford backscattering spectrometry (RBS) is an analytical method able to provide quantitatively elemental information with high accuracy in the near surface region of samples. However, the technique conventionally lacks the required (sub)micron spatial resolution for many semiconductor applications. Firstly, the ion beam current of a highly focused beam is very small, limiting the analytical sensitivity of the measurement. Secondly, the exposure of a sample to a highly focused ion beam readily leads to sample damage, surface sputtering, and accordingly to a measurement error. As a solution to these problems, ensemble RBS is presented whereby multiple devices are measured simultaneously using a broad beam. A judicious choice of the scattering conditions and related data interpretation nevertheless leads to the ability to analyse 3D-devices of micrometre sizes. We demonstrate the potential of this approach through the analysis of atomic species present on the different surfaces of 3D-microfluidic devices. The performance of the technique is demonstrated by the analysis of microfluidic devices after Pt deposition at an oblique angle, and the analysis of the same microfluidic devices after a site-selective deposition of a sub-monolayer of Hf. Further, the performance of ensemble RBS on these structures is compared to the one of microbeam RBS.

1. Introduction

In recent times, the progress in many fields of science and technology has been based on the exploration of small dimensions and new materials [1]. In the semiconductor industry this led to the introduction of 3D device architectures with dimensions in the nm-regime [2,3]. A similar trend has been observed in the field of microfluidics though the devices still have feature sizes in the μm-regime [4]. Evidently, the control of the 3D composition within such devices is essential. Therefore, the important requirements on compositional metrology for such applications are to achieve high spatial resolution to probe the 3D composition within the devices whereby sufficient sensitivity is still achieved. These requirements appear contradictory in nearly all cases where the high spatial resolution is achieved with a highly focused beam, due to the reduced interaction volume. As discussed below, we present a novel approach, termed ensemble RBS, which does provide the required spatial resolution without sacrificing sensitivity.

Rutherford backscattering spectrometry (RBS) is a quantitative

characterization method for the atomic areal density, which has been extensively used for its high traceability [5]. In the last decades the lateral resolution of RBS has been improved by focusing the primary ion beam down to the sub-micrometre regime [6]. However, the advanced beam focus leads to two problems. First, the beam current reduces with beam focussing from tens of nA (for large beams) down to tens of pA for microbeams, or even lower values if focussing is further improved [7–9]. This has an adverse effect on the measurement speed if one targets a certain applied charge for achieving sufficient counting statistics. A second negative consequence of beam focusing is that the beam interaction becomes highly localized and the local fluence is increased substantially compared to broad beam studies, inevitably leading to increased beam damage. Already in the μm-regime this makes the analysis prone to beam damage effects such as sputtering [10].

RBS methodologies have been explored analysing multiple devices simultaneously, to probe the average overall composition of periodic nanostructures [11,12] or the layer-morphology/composition of periodic structures with near micron dimensions [13]. However so far none

of them addressed the problem of also deriving 3D-information. In this paper, we present ensemble RBS as a solution to these problems. Ensemble RBS allows for an average 3D analysis, based on a broad beam directed at an array of identical devices. In the present work the spatial selectivity is achieved by exploiting the 3D-features of the sample in combination with proper choices of the scattering geometry. The use of a mm-size beam and the summation of the signal from an ensemble of identical devices leads to a high signal intensity and improved sensitivity with virtual no detectable beam damage effects.

To validate our methodology, we compare the capabilities of an ensemble RBS analysis to a microbeam RBS analysis on selected samples with microchannel structures which are used in microfluidics [4]. Firstly, we investigate a sample with large 100 μm 3D-features and small aspect ratio for which some selected surfaces are covered with a nm-thick Pt layer. Secondly, we study the determination of sub monolayer Hf-coverages in large (100 μm) and smaller (30 μm) microchannels, as the latter is relevant for understanding the selective atomic layer deposition process [14]. Indeed, to determine the OH-density, these OH groups are chemically transformed into HfO_2 by applying a single cycle of atomic layer deposition (ALD) with $HfCl_4$ and H_2O, and then determining the Hf coverage [15].

2. Materials and methods

The structures used in this work consist of SiO_2/Si microchannels etched in (100) silicon wafers using deep reactive ion etching (DRIE). The etched microchannels are 50 μm deep (D), have a spacing (M) of 30 μm and a nominal width (W) of 30 μm or 100 μm. After the DRIE step the structures were coated with 500 nm thick thermal SiO_2 and etched resulting in a final nominal 100 nm thick oxide layer, as shown in Fig. 1a. The wafer was covered with blocks of 3.3 mm x 2.4 mm, each consisting of microchannels as shown in the optical image in Fig. 1b. The microchannels are connected at their ends with semi-circles such that the whole structure forms one long single microchannel. Fig. 1c provides a top view scanning electron microscopy image of part of the device in which the semi-circle connections of the individual microchannels can be distinguished.

A test sample for our studies was prepared by starting from the 100 μm wide microchannel structures and depositing a Pt layer through evaporation. The Pt layer provides excellent SEM-contrast and a high signal intensity in RBS. During the evaporation, the sample normal is tilted 60(5)° relative to the Pt flux which lead to a Pt deposition on the top surface, on one of the sidewalls, and a small part of the bottom surface only (see Fig. 2a). A quartz micro balance at normal incidence was used to limit the deposition to a 10 nm thick Pt layer. Based on the sample alignment with respect to the platinum flux, we expect the top as well as the covered part of the bottom surface to be coated with 5.0(7) nm, and the sidewall with 8.7(5) nm. Considering the microchannel dimensions and deposition angle, we expect the Pt-covered part at the bottom of the trenches to be 15(15) μm wide. The SEM micrographs obtained after the Pt deposition are shown in Fig. 2b–d and confirm the successful sample preparation. In Fig. 2b, the dark areas indicate the absence of Pt. The brightest areas are the top surface covered with platinum. The grey areas are the bottom surfaces covered with platinum. Moving from Fig. 2c to 2d one can clearly see the effect of the Pt deposition. By measuring the dimensions, with SEM, of several deposition patterns in different microchannels, we estimate the deposition on the bottom surface at 25(2)% of the microchannel area.

To determine the OH-areal density on the surface of the functional microfluidic devices (100 and 30 μm wide microchannels), the etched microchannels were exposed to one ALD cycle of $HfCl_4$ and H_2O to decorate the OH groups with HfO_2. A determination of the Hf-areal density can then be translated directly into the OH areal density [15].

The RBS ensemble experiments were performed using a tandem 6SDH Pelletron accelerator from the National Electrostatics Corporation (NEC) [16]. The end-station consists of a 5-axis goniometer featuring a movable detector in the IBM geometry [17]. The ensemble experiments were performed by using a He^+ beam at an energy of 1.5 MeV with a beam current of 15 nA. The beam spot was confined to an area of 2 mm x 2 mm using slits to avoid probing the semi-circular connections between the individual microchannels. During the experiments, the pressure remained below 10^{-6} mbar. A schematic representation of the experimental geometry used for the macrobeam experiments is depicted in Fig. 3a.

RBS analyses with a focused He-beam were performed at the Ion Beam Centre (IBC) of the University of Surrey using a 2 MV Tandetron from High Voltage Engineering Europe (HVEE), equipped with an OM-150 magnetic quadrupole triplet lens from Oxford Microbeams Ltd [18]. The microbeam scattering chamber is equipped with a tiltable sample holder. The scattering angle was 160° in the Cornell geometry
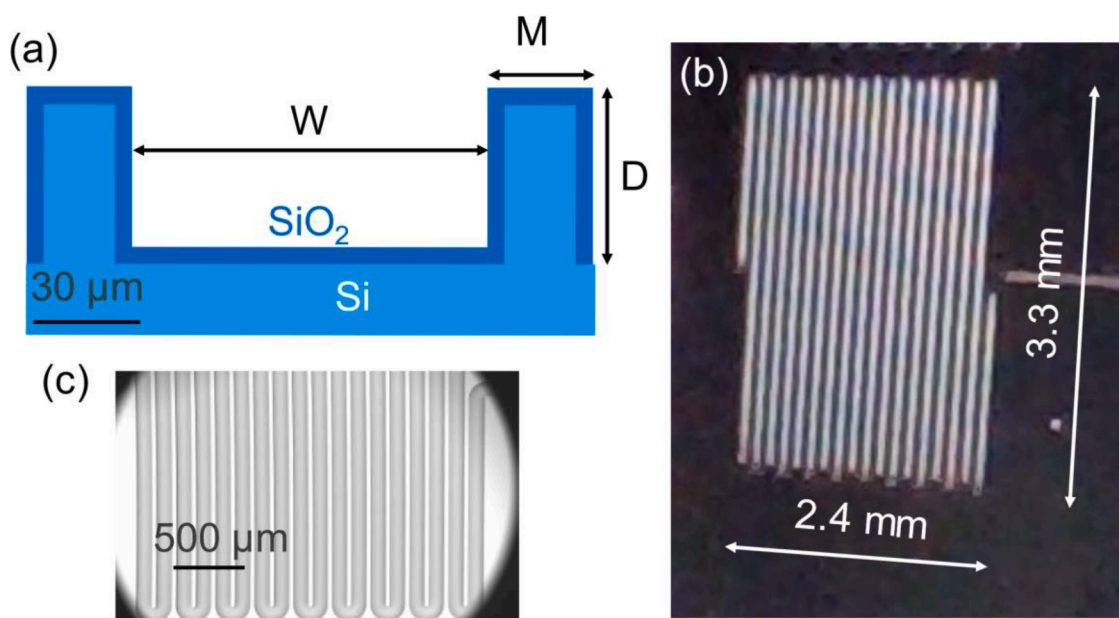
Fig. 1. (a) The cross-section of the microchannel structures (100 μm). (b) Top view optical image of a microchannel device (100 μm). (c) Top view SEM image of part of a microchannel device (100 μm). The white areas are the top surface, while the grey areas are at the bottom of the microchannel.
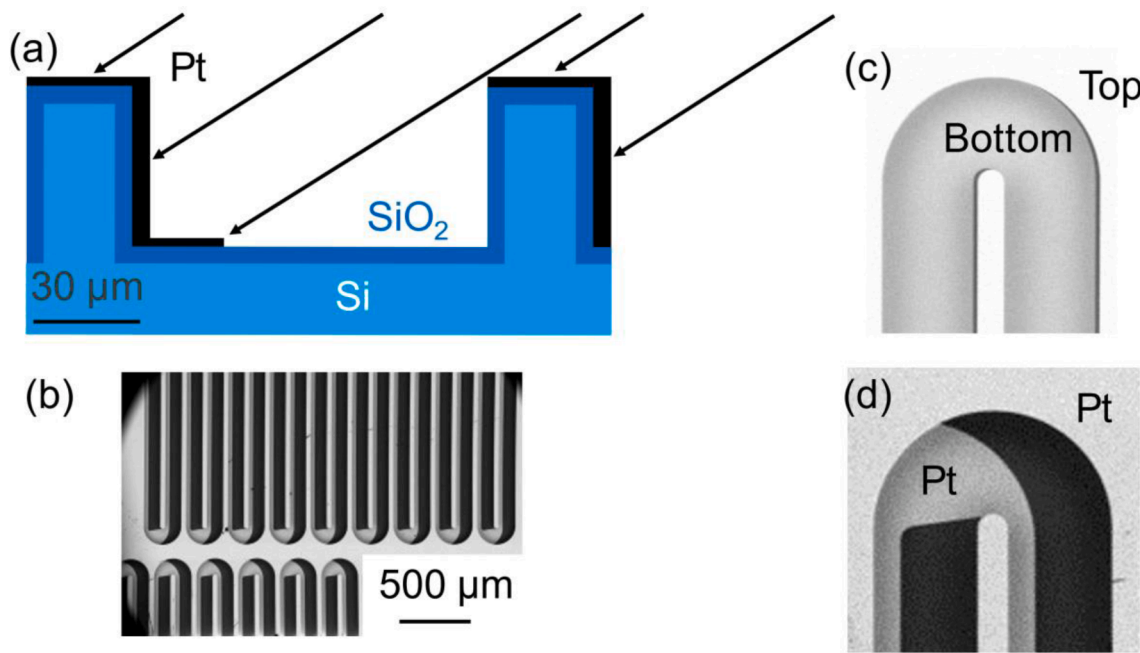
Fig. 2. (a) The cross-section of the microchannel width structures after deposition of Pt at 60° sample tilt. (b) Top view SEM image of the microchannel after deposition of Pt at 60° The dark areas indicate the absence of Pt. The brightest areas are the top surface covered with platinum. The grey areas are the bottom surfaces covered with platinum. (c, d) Top view SEM images of the structures before/after deposition of Pt.
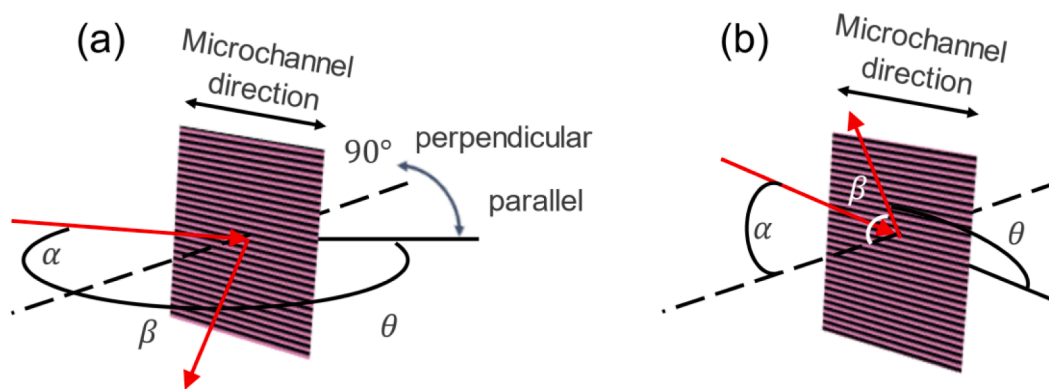

Fig. 3. (a) The experimental geometry in the macroscopic beam set-up. The detector is in the IBM geometry [17]. The microchannels are aligned parallelly or perpendicularly to the scattering plane to expose different parts of the microchannels, as described in the text. (b) The experimental geometry in the microbeam set-up. The detector is in the Cornell geometry [17]. The sample is orientated such that the probing beam can reach the region of interest and such that the structures do not block the backscattering signal.

[17]. The microbeam experiments were performed with a 2 MeV He$^+$ beam, using a beam focused to a size of 10 μm x 10 μm with a beam current of 1 nA. The dimension of the beam was verified by scanning over a Cu grid. During the experiments, the pressure remained below 10^{-6} mbar. A schematic representation of the experimental geometry is shown in Fig. 3b.

The Rutherford backscattering spectra are analysed with SIMNRA [19]. To analyse the spectra that are composed of multiple sub-spectra related to the different surfaces, we constructed a simulator code based on SIMNRA to create and sum up the sub-spectra automatically. The areal density of platinum is converted to a thickness by assuming the bulk mass density of 21.47 g/cm^3.

The scanning electron microscopy (SEM) images were acquired using an Apreo SEM from Thermo Fisher Scientific (TFS). For the SEM imaging, a beam energy of 2 keV with a current of 0.1 nA was used.

3. Ensemble Rutherford backscattering spectrometry

3.1. Ensemble RBS concept

As opposed to the RBS analysis of planar surfaces [17], in the case of 3D-structures the detected signal is strongly affected by the interaction of the incoming or backscattered ions with the topographic features. As illustrated in Fig. 4a, given the micrometre range of MeV energetic ions in solid materials, the signal is effectively blocked when the ions traverse the microscale features of the sample [20]. We will refer to this effect as blocking. Since the studied structures are of the micrometre scale, the stopping effects of the sample topography are so large that there is no need to model the energy loss in detail.

The ensemble RBS concept is illustrated in Fig. 5a–c. The ion beam is *not* focused to the dimensions of the structures but, instead, one takes advantage of the geometrical properties of the sample and the stopping of energetic ions in matter to probe specific regions of the devices. In other words, the sample topography is used to suppress the primary ions
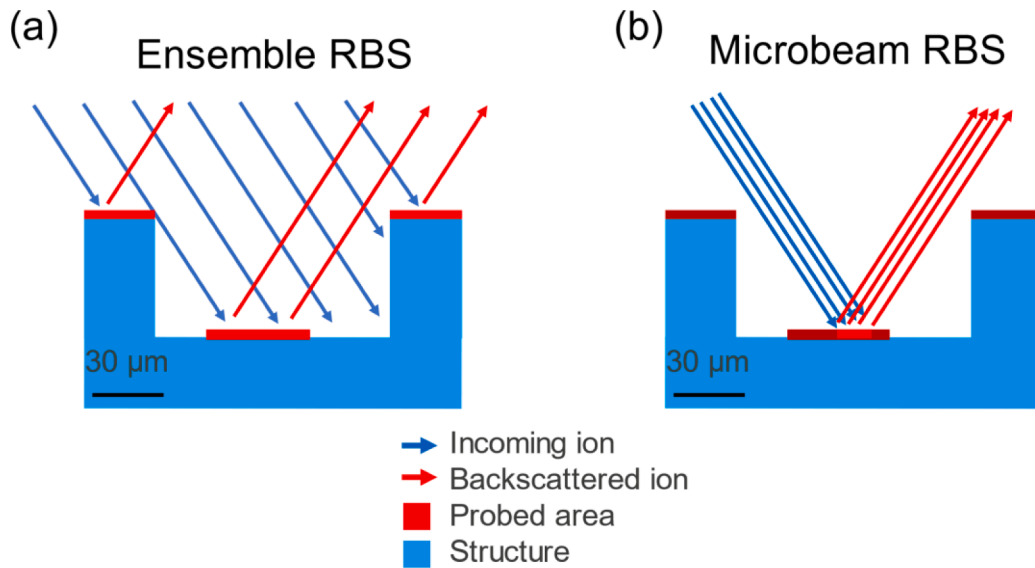
Fig. 4. (a) Blocking effects in ensemble RBS. (b) Blocking effects in microbeam RBS. The red areas indicate regions which can be probed in this geometry.
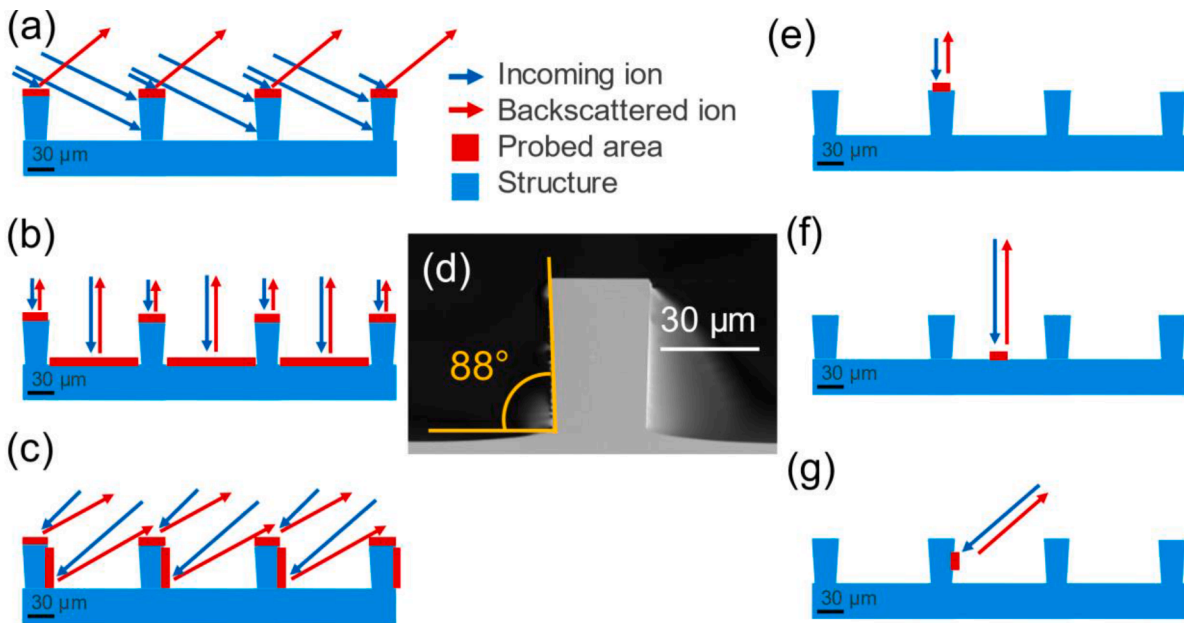

Fig. 5. Concept of the experiments at the microscopic scale, as discussed in the text. The images show the cross-section of the microchannels (100 μm). (a–c) Overview of the performed ensemble experiments. (d) Cross-SEM of the sample indicating the angle of the microchannel walls and the horizontal. (e–g) Overview of the performed microbeam experiments.

from reaching parts of the surface or to prevent the backscattered ions from reaching the detector. The acquisition of RBS spectra in several selected geometries, together with the sample geometry derived from SEM, is sufficient to determine the composition of the different surfaces of the structure.

Under the assumption of complete blocking, the total RBS signal intensity of an element at the sample-vacuum interface (Y) can be expressed as the sum of the partial RBS signal intensities over the different surfaces (Y_i):

$$Y = \sum_{i=1}^{n} Y_i. \tag{1}$$

The partial intensities scale with the number of incident ions on each surface (Q_i), the solid angle (Ω), the RBS scattering cross-section (σ), the

local elemental areal density (N_i) and the inverse of the cosine of the tilt angle relative to the specific surface normal (α_i) [17]:

$$Y_i = \frac{N_i \Omega \sigma Q_i}{\cos(\alpha_i)} \tag{2}$$

Note that the number of incident ions on each surface relates to the total number of incident ions multiplied by the relative projected area of that specific surface normal to the beam. With the relative projected area expressed as (A_i/A), the number of incident ions on each surface is expressed as:

$$Q_i = Q \cdot \frac{A_i}{A} \tag{3}$$

If we know the sample structure, for example from an SEM analysis, then all factors in the above equations are known, except for the local

areal density on each surface. We will show that one can deduce the local areal density on the different surfaces from the combination of RBS spectra taken in different geometries.

For the present microfluidic devices, featuring four different surfaces (top, bottom and two sidewall surfaces), the judicious choice for the measurement geometries is depicted in Fig. 5a–c.

1. In the first geometry (Fig. 5a), the bottom and sidewall surfaces are blocked, to only detect the RBS signal of the top surface. The scattering plane is aligned perpendicular to the microchannels. The sample is tilted at an angle (α) given by the width (W) and depth (D) of the microchannels:

$$\alpha > \arctan\left(\frac{W}{D}\right) \tag{4}$$

to block the bottom surface from the beam. The detector is placed at an angle such that the exit angle ($\beta > 0$) is bigger than zero to block the sidewall from the detector.

2. In the second geometry (Fig. 5b) the RBS spectrum is measured parallel to the microchannels to expose the top and bottom surface to the beam while blocking the sidewalls.

3. In the third geometry (Fig. 5c) the bottom and one sidewall surface are blocked. Only the top surface and one sidewall are probed by aligning the scatter plane perpendicular to the microchannels and by ensuring an exit angle:

$$\beta = -\arctan\left(\frac{W}{D}\right) \tag{5}$$

4. The fourth geometry is the mirrored geometry of the third geometry by rotating the sample by $180°$, hence probing the top surface and the other sidewall.

From the experiment in the first geometry, we determine the areal density on the top surface. For the other experiments, more than one region contributes to the spectra. We use Eqs. (1)–(3) to further determine the local areal densities of the other surfaces as summarised in Table 1. Notice that N_i is the average areal density on the top, bottom, or sidewall surface. If the surface is only partially covered, as is the case for the bottom surface of the test structures, the reported areal density is an average over the entire surface.

3.2. Ensemble RBS experimental results and discussion

We first analyse the Pt demonstrator structures to test the methodology. The spectra are obtained with a nominal charge of 12.5 μC whereby the Si oxide signal is used to estimate the charge · solid-angle product and whereby the amorphous nature of the oxide precludes any channelling effects [17,21]. Based on a spectrum taken in the non-patterned area the areal density of Pt is 31.3(1.6) 10^{15} at/cm^2, which corresponds to a thickness of 4.7(2) nm, in good agreement with the anticipated thickness of 5 nm. Subsequently, the four different

experimental geometries were used to disentangle the Pt areal density on the four different surfaces. The Rutherford backscattering spectra probing the top, the top and bottom, and the top and one of the sidewall surfaces are shown in Fig. 6. The low-energy signal corresponds to He ions scattering from the substrate whereas the high-energy signal corresponds to the He ions scattering from Pt. The spectra shown in Fig. 6c and 6d correspond to the third and fourth geometry, exposing the left and right sidewalls, respectively. It is readily seen in Fig. 6c and 6d that the Pt signal is visibly less intense when the sidewall without platinum deposition is probed. The remaining Pt signal is due to the coverage of the top surface.

From the analysis of the Rutherford backscattering spectra, we obtain the following results. The top surface has a Pt areal density corresponding to 4.6(3) nm. The thickness of Pt on the covered sidewall is 8.1(1.1) nm. The bottom surface has an average Pt areal density of 1.5(2) nm. The thickness of Pt on the uncovered sidewall is 0.2(4) nm. The ensemble result for the average areal density of Pt for the structures is shown in Table 2. The reported uncertainties are estimated as discussed in the next section. The experimental standard deviation derived from repeated measurements is found to be 0.07 nm for the top, 0.02 nm for the bottom, 0.17 nm for the covered sidewall, and 0.04 nm for the uncovered sidewall.
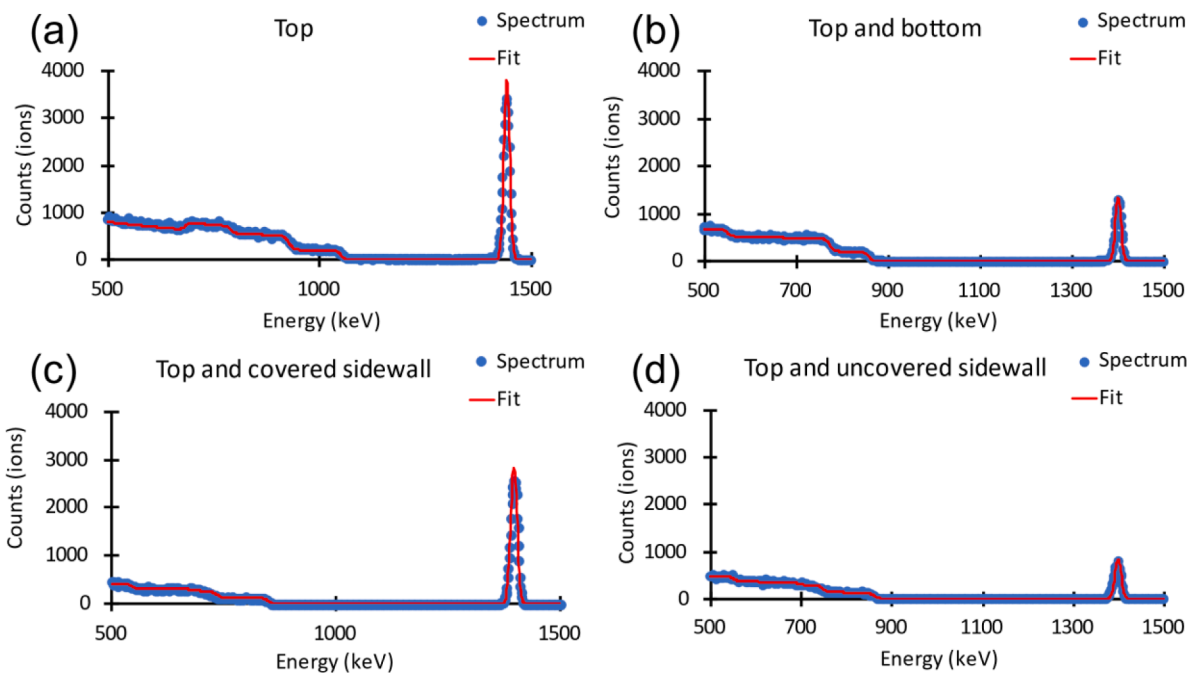
The top and sidewall areal densities correspond well with the nominally deposited values of 5.0(7) nm and 8.7(5) nm, respectively. Notice that, although only part of the bottom surface is covered, the ensemble methodology averages the thickness over the bottom surface. To be able to compare the ensemble results, we average the nominally deposited values using the Pt coverage from the covered bottom surface and the ratio of the covered to uncovered bottom area from SEM which leads to 1.3(2) nm. Moreover, the extracted areal density on the uncovered sidewall is small and zero within the uncertainty. This is because the areal density on the sidewalls is calculated taking the expected yield of the top surface into account (Table 1). The results convincingly establish ensemble RBS as a viable technique to characterize high-Z layers in micrometre sized periodic 3D structures.

The previous example demonstrated the 3D-resolving power of our approach on a nanometre thick Pt layer which is of course advantageous for RBS. In the following we focus also on the improved sensitivity by analysing a set of microfluidic devices that underwent one cycle of atomic layer deposition using HfCl$_4$ and H$_2$O. Based on a spectrum taken in the non-patterned area the areal density of Hf is as small as 0.288(16) 10^{15} atoms/cm^2. A similar procedure as described above was used to acquire four independent spectra for both the 100 μm and 30 μm width structures. The ensemble result for the average areal density of Hf for both structures is shown in Table 3. The experimental standard deviation derived from repeated measurements is 0.02 10^{15} atoms/cm^2 for the top, 0.03 10^{15} atoms/cm^2 for the sidewall and bottom surface. The similarity in coverages (top, bottom, sidewall), is characteristic for the conformal deposition using atomic layer deposition and indicates that the OH areal density was similar for the different surfaces.

3.3. Uncertainty budget ensemble RBS

The reported areal densities from the ensemble RBS analysis are derived from multiple and off-normal experiments. Here we discuss the propagated uncertainty budget for the ensemble analysis. It includes the regular uncertainties for RBS, such as the counting statistical uncertainty (1–6%), the stopping power of SiO$_2$ (5%), the tilt angle (0.5°) and the scattering angle (0.5°) [17]. In addition, for ensemble RBS one must account for the following uncertainties.

First, an error is introduced by assuming that all devices are identical and fully probed. Due to the finite beam/device dimensions it is likely that at the edge of the beam only a part of the devices is analysed. As explained in Section 3.1 the extracted product of charge and solid angle using the internal normalization on the Si oxide signal needs to be scaled as summarised in Table 1. Here we implicitly assumed that the

Table 1
Equations for the local average areal density (N) and for the dose solid angle product (ΩQ) on the different surfaces of the microfluidic devices. The index specifies in which geometry the values need to be measured or evaluated. M is the spacing of the microchannels.

Surface	N	ΩQ
Top	$\dfrac{Y_1 \cos(\alpha_1)}{\sigma_1 \Omega Q_{top}}$	ΩQ_1
Bottom	$\dfrac{Y_2 \cos(\alpha_2)}{\sigma_2 \Omega Q_{bottom}} - N_{top}\dfrac{M}{W}$	$\Omega Q_2 \dfrac{W}{P}$
Sides	$\dfrac{Y_{3/4} \sin(\alpha_{3/4})}{\sigma_{3/4} \Omega Q_{side}} - N_{top}\dfrac{M}{D}$	$\Omega Q_{3/4} \dfrac{D \tan(\alpha_{3/4})}{M + D \tan(\alpha_{3/4})}$

Fig. 6. Ensemble RBS spectra taken in the geometries shown in Fig. 5 sensitive to the top surface (a), to the bottom and top surface (b), to the covered sidewall and top surface (c), and to the uncovered sidewall and top surface (d) of the Pt demonstrator sample. Notice the large difference in Pt signal between spectrum (c) and (d). The spectra are fitted using the simulator for microstructures discussed in the text.

Table 2
Summary of the measured results for the Pt areal density of the set of test structures.

	Microbeam (nm)	Uncertainty (nm)	Ensemble (nm)	Uncertainty (nm)
Pt demonstrator				
Top	4.9	0.3	4.6	0.3
Covered bottom	4.9	0.3		
Uncovered bottom	0			
Average bottom			1.5	0.2
Covered sidewall	8.2	0.6	8.1	1.1
Uncovered sidewall	0		0.2	0.4

Table 3
Summary of the measured results for the Hf areal density of both sets of 100 μm and 30 μm structures.

	Microbeam(10^{15} at/cm^2)	Uncertainty(10^{15} at/cm^2)	Ensemble(10^{15} at/cm^2)	Uncertainty(10^{15} at/cm^2)
100 μm microchannel				
Top	0.197	0.017	0.294	0.018
Bottom	0.191	0.016	0.26	0.03
Sidewall	0.21	0.02	0.29	0.06
	Microbeam (10^{15} at/cm^2)	Uncertainty (10^{15} at/cm^2)	Ensemble (10^{15} at/cm^2)	Uncertainty (10^{15} at/cm^2)
30 μm microchannel				
Top	0.186	0.016	0.31	0.02
Bottom	0.207	0.016	0.27	0.06
Sidewall			0.27	0.06

contributing surfaces are receiving an equal number of ions for each device. This error can result in an under- as well as an over-estimation of the local elemental areal density on the bottom and sidewall surfaces. By assuming a homogenous beam, the error scales with the pitch to beam diameter as the inverse ratio corresponds to the number of lines probed. The largest deviation possible occurs when one probes half a micro-channel whereas no error is made when an integer number of micro-channels are probed. When using a beam spot of 2 mm, this results in an error below 4% and 1.5% on the scaled products of charge and solid angle for the 100 μm and 30 μm structures, respectively.

Secondly, we investigate if the assumption that the blocking effects

are absolute can result in a bias on the local elemental areal density on the different surfaces. This assumption does not hold strictly at the edges of the top surface of the structure (Fig. 4(e–g)) which leads to a contribution to the experimental yield for the Hf or Pt signals which is unaccounted for. To be able to distinguish signals in RBS the energy difference of the signals must be larger than the energy width of the signals. According to Eq. (3) the systematic uncertainty scales with the charge on the blocked surface of which the backscattered ions lose an energy lower than that of the energy width. Using the stopping power of SiO_2 and assuming uniform coverage, this results in a negligible bias below 1% on the extracted yields for the studied structures.

Thirdly, deviations on the experimental geometry can result in an additional error. In the first geometry (Fig. 4e) the additional error can be avoided. For the second geometry (Fig. 4f) the deviations on the sample rotation angle can cause a partial blocking of part of the bottom surface. This results in a negligible bias below 1% on the scaled products of charge and solid angle for the 100 μm and 30 μm structures. In the third and fourth geometry (Fig. 4g) eventual deviations on the exit angle can lead to exposing part of the bottom surface or blocking part of the sidewall surface. We estimate the relative uncertainty on the scaled products of charge and solid angle due to the uncertainty on the exit angle as 7% and 2% for the 100 μm and 30 μm structures, respectively.

The above errors define the regime in which the ensemble methodology works best. The first and third error prevent the application of ensemble RBS to very large devices above 100 μm. The second error limits the applicability of ensemble RBS to devices not smaller than 1 μm. For smaller devices the assumption that the ions are fully stopped when encountering the structures is no longer valid, and a more advanced data treatment is needed.

4. Comparison of microbeam and ensemble RBS

4.1. Microbeam RBS experimental results and discussion

To validate our results, we also analysed a set of selected samples with Microbeam RBS. In this case the composition of planar surfaces is determined locally by detecting the RBS spectra while scanning the focussed beam over the sample surface [18]. In this way elemental maps can be constructed to show the lateral and in-depth compositional differences across the sample. However, as discussed in Section 3.1, in the case of (3D) vertically structured samples, the detected signal is strongly affected by the interaction of the incoming or backscattered ions with the topographic features (Fig. 4b).

If one can probe an area of the sample without blocking, then the backscattering signals originate solely from the exposed area and may be interpreted as a conventional RBS spectrum from a layered sample such that the standard data interpretation applies. Note that this methodology is only possible if the probing ion beam can be focused down to or below the feature size. This has been achieved in Fig. 5e and 5f by aligning the beam at normal incidence to the top and to the bottom surfaces, respectively. Conversely, the sidewalls are exposed to the beam by tilting the sample at 45° as can be seen in Fig. 5g.

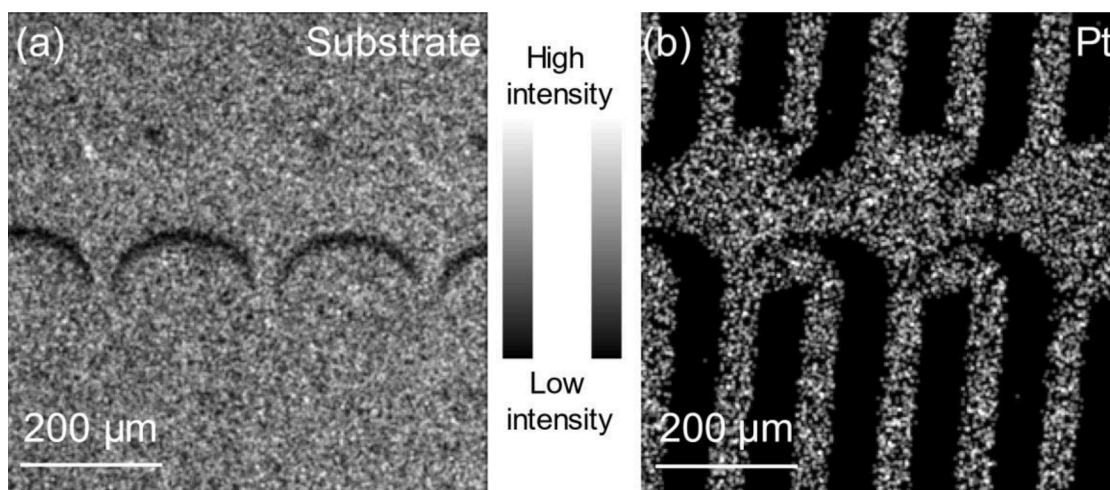Referring to the Pt demonstrator structures, the microchannels are aligned parallel to the RBS scattering plane to avoid blocking effects while probing the microchannels. Yet, the blocking effects (Fig. 7a) are still apparent as dark spots in the microbeam maps in the semi-circular regions of the microchannels. The dark spots can be used to position the beam at a specific location on the sample: on the top, the bottom, or the sidewall surface of the microchannel. As can be seen in Figs. 7a and 1b, c, the blocking effects align perfectly with the shape of the structures. The map shows that part of the bottom surface is covered with Pt (Fig. 7b) as is also visible in the top-view SEM micrographs (Fig. 2b and 2d).

The RBS spectra obtained on the platinum demonstrator sample are shown in Fig. 8. The spectra are obtained with a nominal charge of 500 nC whereby the Si oxide signal is used to estimate the charge · solid-angle product. Based on a spectrum taken in the non-patterned area, the areal density of Pt corresponds to a thickness of 4.6(3) nm. The RBS spectra taken on the top, the bottom, and the sidewall surfaces are shown in Fig. 8. The low-energy signal corresponds to He ions scattering from the substrate whereas the high-energy signal corresponds to the He ions scattering from Pt. The microbeam result for the Pt areal density for these structures is shown in Table 2 together with the ensemble results for comparison. The top and covered bottom surface have a Pt areal density corresponding to 4.9(3) nm. The thickness of Pt on the covered sidewall is 8.2(6) nm. The Pt on the uncovered sidewall and bottom surface is below the detection limit of 0.004 nm.

The reported uncertainties include the counting statistical uncertainties of the Pt signal (1%) and Si oxide signal (3%) used for the estimation of the charge solid angle product as well as the propagated uncertainties from the stopping power of SiO_2 (5%) and from the uncertainty on the sample tilt angle (0–4%) [17]. The experimental standard deviation derived from repeated measurements at various locations is found to be 0.15 nm for the top and covered bottom surface, and 0.5 nm for the sidewall. The experimental standard deviation for the Pt-covered sidewall being slightly higher than expected is attributed to a small mispositioning of the beam.

Fig. 9 displays a comparison between the nominal and measured Pt thicknesses using microbeam RBS and ensemble RBS. As discussed in Section 3.2 the ensemble methodology averages the thickness over the bottom surface. To be able to compare the microbeam to ensemble results, we averaged the microbeam result using the Pt coverage from the top and covered bottom surface, as determined with microbeam RBS, and the ratio of the covered to uncovered bottom area from SEM.

The same approach as used for the Pt-containing sample is used to selectively probe the areal density of the different surfaces of the structures treated with one $HfCl_4/H_2O$ ALD cycle. Since the areal density

Fig. 7. Normal incidence RBS maps of the substrate signal (a) and of the integrated Pt signal (b) of the Pt demonstrator structures. The RBS map (a) displays blocking effects in the semi-circular connections of the microchannels which can be used to position the beam on the region of interest, i.e., the top, bottom, or sidewall surface. The Pt map (b) correlates well with the SEM image (Fig. 2a, b).
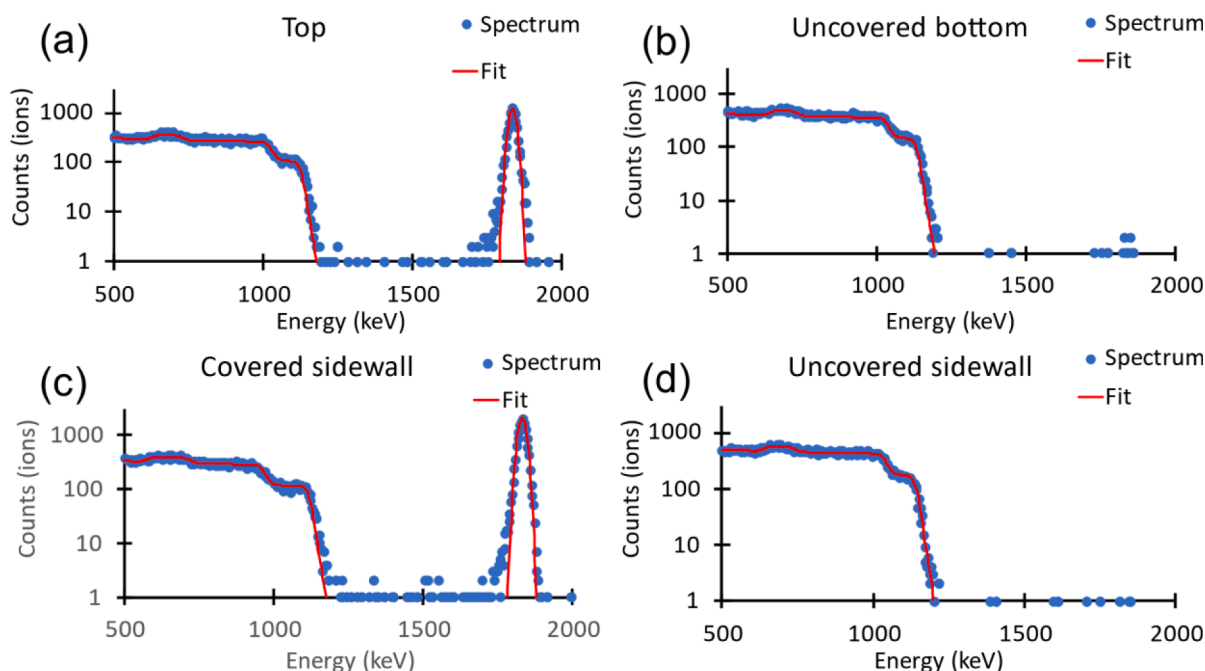
Fig. 8. Local microbeam RBS spectrum taken on top of the microchannel wall (a), at the uncovered bottom of the microchannel (b), on the covered sidewall (c), and the uncovered sidewall (d) of the Pt demonstrator sample. The spectra are plotted in logarithmic scale. The spectra are fitted using SIMNRA [20].
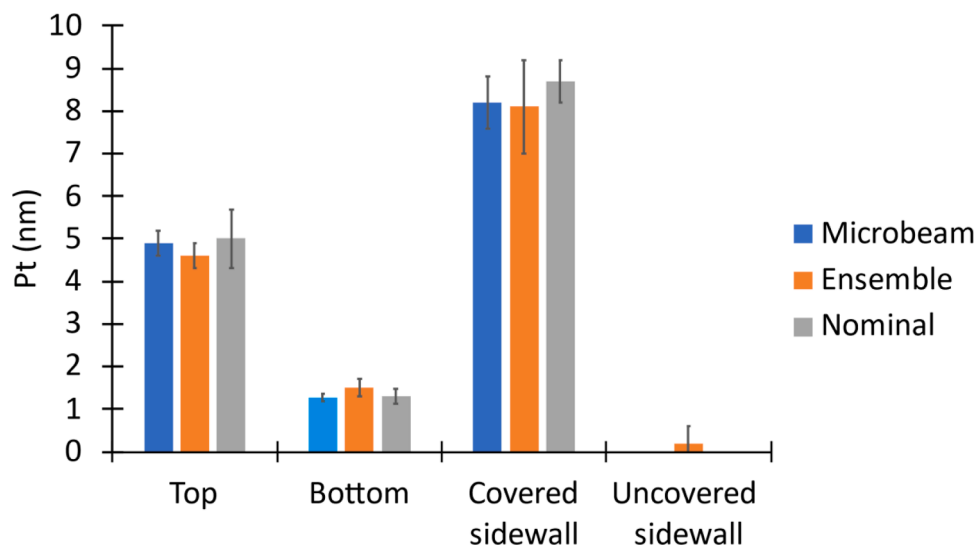
Fig. 9. Experimental results for the Pt areal density on the different surfaces of the demonstrator sample using microbeam and ensemble RBS, compared to the nominal areal density of Pt. The data bar highlighted in light blue is an estimated average using the Pt coverage from the top and covered part of the bottom surface determined using microbeam RBS and the ratio of the covered to uncovered bottom area from SEM as described in the text.

of Hf is much lower than the platinum areal density, a nominal charge of 2 μC is needed to get sufficient counting statistics on the Hf signal. First, a point spectrum next to the structures is measured as a reference, resulting in an Hf areal density of 0.189(16) 10^{15} atoms/cm^2. The microbeam results for the areal density of Hf for both structures are shown in Table 3 together with the ensemble results for comparison. The reported uncertainty is dominated by the statistical uncertainty (10%). The experimental standard deviation on the values for the three surfaces is found to be 0.02 10^{15} atoms/cm^2. At first sight, there is a disparity between the results obtained with ensemble RBS and microbeam RBS, the latter reporting lower values.

4.2. Beam damage effects

A possible explanation for this discrepancy could be beam-induced damage, which is a known concern when performing microbeam experiments. Specifically, the sputtering of surface atoms must be considered when determining sub-monolayer coverages and ultrathin layers, as the related material loss may lead to large relative experimental errors. To estimate the importance of this effect we studied the material loss due to the He irradiation of the Hf areal density. We present results of consecutive microbeam experiments on a blanket film SiO$_2$/Si sample, treated with one HfCl$_4$/H$_2$O ALD cycle, irradiated at 45° (with respect to the sample normal) with 2 MeV He ions (Fig. 10). The measurements are performed as twelve consecutive acquisitions with a nominal charge of 500 nC, without moving the beam or sample in
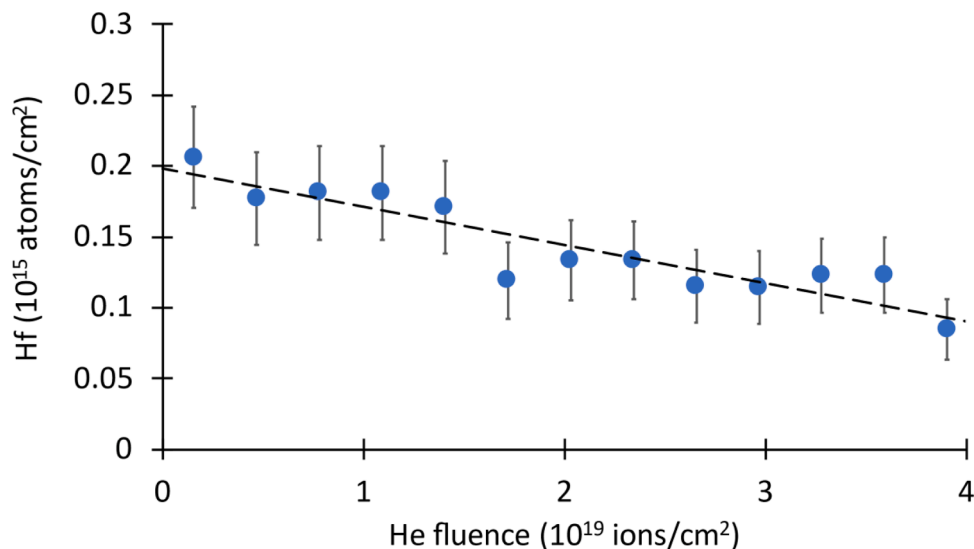
Fig. 10. The Hf areal density as determined with RBS in function of He fluence.

between. The sputter yield (Y_s) is then estimated from the slope of the areal density (N) as a function of the applied nominal fluence (Q/A) [10]:

$$N = N_0 - \frac{Y_s Q}{A} \qquad (6)$$

From the linear fit in Fig. 10, we deduce that the probability to sputter a hafnium atom from the surface is 2.6(5) 10^{-6} per incoming He ion. Considering the experimentally determined sputter yield we estimate that the microbeam analysis underestimates the Hf areal densities by 0.07(2) 10^{15} atoms/cm², implying a significant correction to the measured value (~30%). This is a concern when using microbeam RBS for the absolute quantification of sub-monolayer areal densities. When dealing with the analysis of the nanometre thick Pt layers, the effect remains relatively less severe. On the other hand, for ensemble RBS, given the much larger area (~10^4) probed, the impact of sputtering remains negligible for both Hf and Pt areal densities.

Fig. 11 displays a comparison between the measured Hf thicknesses using microbeam RBS, after correcting for the sputtered material, and ensemble RBS. As expected, the disagreement between the results obtained with ensemble RBS and microbeam RBS disappears after correcting for the sputtered material.

4.3. Practical difficulties with microbeam RBS

Even though the nominal beam spot specification is below 10 μm x 10 μm, we encountered difficulties to probe microchannels with a width of 30 μm. In this case, the finite beam diameter, and the high aspect ratio of the microchannels (50 μm deep, 30 μm wide) hinder the analysis of the sidewall. It is found that the maximum tilt angle imposed by the sample topography is 35° when measuring in the middle of the sidewall. In this case the footprint of the beam is expected to double in size. Furthermore, there is a finite uncertainty on the beam position and the beam is not infinitely sharply bordered. We ascertain that it is very difficult to avoid contributions of the area surrounding the region of interest. For this, we have not succeeded to characterise the sidewall by means of microbeam RBS for the microfluidic devices with a width of 30 μm.
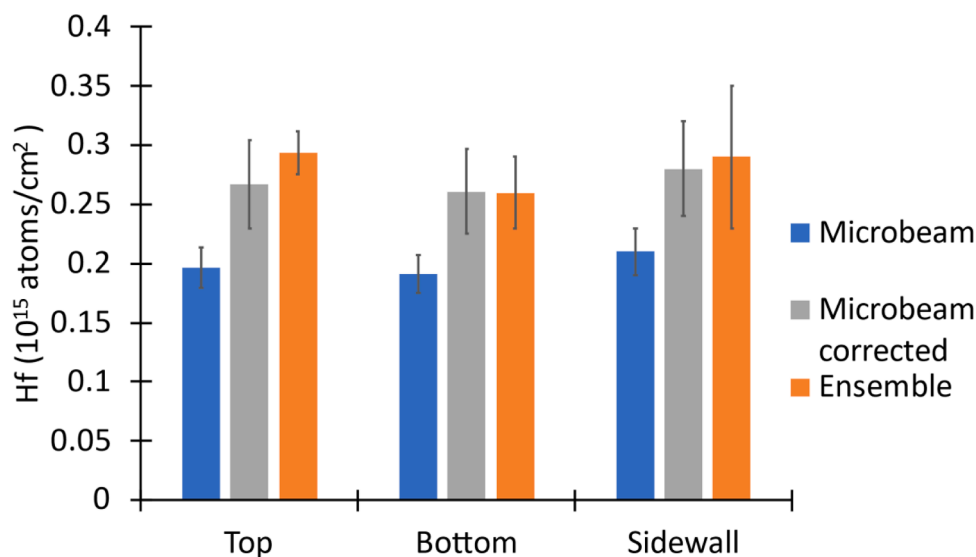

Fig. 11. Experimental results on the Hf areal density on the different surfaces of the 100 μm width microchannels using Microbeam and Ensemble RBS. We also show the estimated values for Microbeam RBS after correcting for the sputtering of the target material.

5. Conclusion

We have presented ensemble RBS to probe the site-specific elemental areal density of high-Z atomic species on the surface of microfluidic devices. The method allows one to determine the areal density for the top, the bottom, as well as the sidewall surfaces of microchannels. We have used microbeam RBS to validate the results. The concept of ensemble RBS by exploiting the stopping effect of ions in the topography of the sample provides a solution to measure the sub-monolayer areal density in narrow 3D-microchannels. The ensemble RBS approach allows to obtain statistically relevant data by averaging over many devices. This implies having a high sensitivity and measurement statistics by averaging over many structures as well as a faster analysis time. On the other hand, due to the need for multiple and off-normal experiments to derive these areal densities there are additional sources of uncertainty which need to be considered. Ultimately, ensemble RBS allows an average value over many devices and is insensitive to local non-homogeneities.

Declaration of Competing Interest

The authors declare that they have no known competing financial interests or personal relationships that could have appeared to influence the work reported in this paper.

References

[1] M.M. Heyns, M.M. Meuris, M.R. Caymax, Ge and III/V as enabling materials for future CMOS technologies, ECS Trans. 3 (2006) 511, https://doi.org/10.1149/1.2355848.

[2] S. Natarajan, et al., A 14 nm logic technology featuring 2nd-generation FinFET, air-gapped interconnects, self-aligned double patterning and a 0.0588 μm2 SRAM cell size, in: Proceedings of the IEDM, IEEE, 2014, https://doi.org/10.1109/IEDM.2014.7046976, 3.7.1-3.7.3.

[3] I. Markov, Limits on fundamental limits to computation, Nature 512 (2014) 147–154, https://doi.org/10.1038/nature13570.

[4] A.G. Niculescu, C. Chircov, A.C. Bîrcă, A.M. Grumezescu, Fabrication and applications of microfluidic devices: a review, Int. J. Mol. Sci. 22 (2021) (2011), https://doi.org/10.3390/ijms22042011.

[5] C. Jeynes, N.P. Barradas, E. Szilágyi, Accurate determination of quantity of material in thin films by rutherford backscattering spectrometry, Anal. Chem. 84 (14) (2012) 6061–6069, https://doi.org/10.1021/ac300904c.

[6] A.G. Ponomarev, A.A. Ponomarov, Beam optics in nuclear microprobe: a review, Nucl. Instrum. Methods Phys. Res. B 497 (2021) 15–23, https://doi.org/10.1016/j.nimb.2021.03.024.

[7] G.W. Grime, M. Dawson, M. Marsh, I.C. McArthur, F. Watt, The Oxford submicron nuclear microscopy facility, Nucl. Instrum. Methods Phys. Res. B 54 (1991) 52–63, https://doi.org/10.1016/0168-583X(91)95490-5.

[8] F. Watt, J.A. van Kan, I. Rajta, A.A. Bettiol, T.F. Choo, M.B.H. Breese, T. Osipowicz, The National University of Singapore high energy ion nano-probe facility: performance tests, Nucl. Instrum. Methods Phys. Res. B 210 (2003) 14–20, https://doi.org/10.1016/S0168-583X(03)01003-6.

[9] Y. Yao, J.A. van Kan, Automatic beam focusing in the 2nd generation PBW line at sub-10 nm line resolution, Nucl. Instrum. Methods Phys. Res. B 348 (2015) 203–208, https://doi.org/10.1016/j.nimb.2014.12.066.

[10] J.A. Cookson, Specimen damage by nuclear microbeams and its avoidance, Nucl. Instrum. Methods Phys. Res. B 30 (1988) 324–330, https://doi.org/10.1016/0168-583X(88)90020-1.

[11] G. Laricchiuta, W. Vandervorst, I. Vickridge, M. Mayer, J. Meersschaut, Rutherford backscattering spectrometry analysis of InGaAs nanostructures, J. Vac. Sci. Technol. A 37 (2019), 020601, https://doi.org/10.1116/1.5079520.

[12] O.M.I. Sangrador, J. Rodríguez, A. Rodríguez, T. Kling, A. Franco, N. Barradas, and C. Ballesteros, Growth by LPCVD, crystallization and characterization of SiGe nanoparticles for nanoelectronic devices, Phys. Status Solidi (A), 203 (2006) 1284–1290. 10.1002/pssa.200566105.

[13] Z. Zolnai, N. Nagy, A. Deák, G. Battistig, E. Kótai, Three-dimensional view of the shape, size, and atomic composition of ordered nanostructures by Rutherford backscattering spectrometry, Phys. Rev. B 83 (2011), 233302, https://doi.org/10.1103/PhysRevB.83.233302.

[14] W.L.W. Hau, D.W. Trau, N.J. Sucher, M. Wong, Y. Zohar, Surface-chemistry technology for microfluidics, J. Micromech. Microeng. 13 (2003) 272, https://doi.org/10.1088/0960-1317/13/2/315.

[15] L. Nyns, A. Delabie, M. Caymax, M.M. Heyns, S. Van Elshocht, C. Vinckier, S. De Gendt, HfO₂ atomic layer deposition using HfCl₄ / H₂O: the first reaction cycle, J. Electrochem. Soc. 155 (2008) G269, https://doi.org/10.1149/1.2980427.

[16] J. Meersschaut, W. Vandervorst, High-throughput ion beam analysis at imec, Nucl. Instrum. Methods Phys. Res. B 406 (2017) 25–29, https://doi.org/10.1016/j.nimb.2017.01.005. A.

[17] W.K. Chu, J.W. Mayer, M.A. Nicolet, Backscattering Spectrometry, Academic Press, 1978, https://doi.org/10.13140/RG.2.1.1948.0807.

[18] A. Simon, C. Jeynes, R.P. Webb, R. Finnis, Z. Tabatabaian, P.J. Sellin, M.B. H. Breese, D.F. Fellows, R. van den Broek, R.M. Gwilliam, The new Surrey ion beam analysis facility, Nucl. Instrum. Methods Phys. Res. B 219-220 (2004) 405–409, https://doi.org/10.1016/j.nimb.2004.01.091.

[19] M. Mayer, SIMNRA, a simulation program for the analysis of NRA, RBS and ERDA, AIP Conf. Proc. 475 (1999) 541–544, https://doi.org/10.1063/1.59188.

[20] M.J. Berger, J.S. Coursey, M.A. Zucker, J. Chang, Stopping-Power & Range Tables for Electrons, Protons, and Helium Ions, v2, NIST, 2017, https://doi.org/10.18434/T4NC7P.

[21] M. Bianconi, F. Abel, J.C. Banks, A.C. Font, C. Cohen, B.L. Doyle, R. Lotti, G. Lulli, R. Nipoti, I. Vickridge, D. Walsh, E. Wendler, The Si surface yield as a calibration standard for RBS, Nucl. Instrum. Methods Phys. Res. B 161-163 (2000) 293–296, https://doi.org/10.1016/S0168-583X(99)00927-1.